mater.scichina.com link.springer.com

Sci China Mater 2025, 68(10): 3549–3556
https://doi.org/10.1007/s40843-025-3512-2

Chloride-passivated lead sulfide thin film for high-performance extended short wavelength infrared photodiode

Shaoheng Xu[1†], Sen Li[1,2†], Wenyu Zhang[3], Hao Luo[4], Ruiming Li[5], Qianqian Lin[5], Haisheng Song[1], Jiajun Luo[1*] and Jiang Tang[1,2,3,6*]

ABSTRACT **Liquid-phase chemically deposited lead sulfide as a narrow-bandgap semiconductor holds great potential for extended short-wavelength infrared sensing. However, lead sulfide thin films typically contain massive sulfur vacancies and oxygen impurities, which form during chemical deposition, leading to inferior device performance. Here, for the first time, we report on the *in-situ* passivation of lead sulfide polycrystalline film with chloride ions as an additive during liquid-phase chemical deposition. Due to the similar ionic radius of chloride ions to sulfur ions and their ability to coordinate with lead ions, the addition of chloride ions effectively reduces sulfur vacancy and oxygen-in-sulfur defect densities. The reduction of bulk defect densities lowered the dark current density of homojunction photodiodes made from the passivated film by more than threefold. The photodiode exhibited a high responsivity of 0.79 A/W at 2.5 μm and a fast response speed of 19.6 μs. At room temperature, the 1 mm^2 photodiodes exhibited a resistance-area product of 8.78 Ω cm^2 and a specific detectivity of 8.79 × 10^9 Jones at 2.5 μm, among the best-reported performance of lead sulfide bulk thin film photodiode. At 80 K, the resistance-area product was 6.16 kΩ cm^2. This research paves a new path for high-performance extended short-wavelength infrared photodetector.**

Keywords: lead sulfide (PbS), extended short wavelength infrared (eSWIR), photodetector, chlorine incorporation, defect passivation

INTRODUCTION

The extended short wavelength infrared (eSWIR) band, spanning from 2 to 3 μm, is of great significance due to its unique properties: eye safety, long-range visibility, strong anti-jamming ability, and fine molecule absorption [1–6]. Lead sulfide (PbS) is a typical narrow bandgap semiconductor that is intrinsically sensitive to infrared light up to 2.95 μm at 300 K, covering the full eSWIR range [7–11]. Additionally, PbS photodetectors can operate at elevated temperatures, with low dark current due to an inherently low Auger recombination rate [12]. Therefore, exploring high-performance PbS film photodetectors is of great importance.

Liquid-phase chemical deposition has been the most widely adopted method for fabricating lead sulfide polycrystalline thin film due to its process simplicity, tailorable optoelectronic properties, high specific detectivity, and facile monolithic integration [13]. Furthermore, the versatility and conformality of the liquid-phase chemical deposition process enable film fabrication on non-planar surfaces, such as biomimetic electronic devices. This capability enables the sensor with a wide-angle field of view, low aberrations, high motion acuity, and a near-infinite depth of field [14–17]. However, PbS photodetectors often suffer from high dark current density and slow response, primarily due to sulfur-related defects, i.e., sulfur vacancies, and oxygen-in-sulfur defects, formed during the chemical deposition process. Typically, the liquid-phase chemically deposited lead sulfide polycrystalline thin films exhibit a carrier concentration of over 10^{17} cm^{-3} [18–25]. Thus, eliminating these defects is essential to enhance the performance of PbS bulk thin-film photodetectors.

Chloride ions, with an ionic radius of 176 pm (close to the 179 pm of sulfur ions), are ideal candidates for passivating sulfur vacancies. Additionally, chloride ions can coordinate with lead ions and the crystalline surface of lead sulfide. The characteristics suggest that chloride ions could affect the PbS crystalline growth and passivate the sulfur-related defects without causing significant crystal lattice distortion.

Herein, we introduce an *in-situ* chloride additive during chemical bath deposition to reduce the sulfur vacancy and oxygen-in-sulfur (O_S) defect densities. The resulting PbS polycrystalline thin films exhibited high crystallinity and preferred orientation along (200) facets. X-ray photoelectron spectroscopy (XPS) confirmed that adding sodium chloride (NaCl) significantly reduced oxygen content and nearly eliminated oxygen-in-sulfur defects. Consequently, the dark current of PbS p-n homojunction devices was reduced by threefold, and the zero-

[1] Wuhan National Laboratory for Optoelectronics (WNLO), Huazhong University of Science and Technology (HUST), Wuhan 430074, China
[2] Optical Valley Laboratory, Wuhan 430074, China
[3] School of Optical and Electronic Information (OEI), Huazhong University of Science and Technology (HUST), Wuhan 430074, China
[4] School of Integrated Circuits, Huazhong University of Science and Technology (HUST), Wuhan 430074, China
[5] Key Lab of Artificial Micro- and Nano-Structures of Ministry of Education of China, School of Physics and Technology, Wuhan University, Wuhan 430072, China
[6] Wenzhou Key Laboratory of Microwave Communication Materials and Devices, Wenzhou Advanced Manufacturing Institute of Huazhong University of Science and Technology, Wenzhou 325035, China
† Equally contributed to this work.
* Corresponding author (email: luojiajun@mail.hust.edu.cn; jtang@mail.hust.edu.cn)

 © Science China Press 2025

bias specific detectivity increased to 8.79×10^9 Jones at 2.5 μm and 300 K.

EXPERIMENTAL SECTION

The PbS thin film was deposited on fluorine-doped tin oxide (FTO) glass substrate from the mixture of 20 mL $Pb(NO_3)_2$ (18 mmol/L), 100 μL $CS(NH_2)_2$ (0.1 mol/L) and 0.25 g NaOH solutions. Before deposition, the pH value of the mixture solution was adjusted to 11.3 by 30% HNO_3. NaCl was added to the precursor solution to improve the PbS film quality. Before the deposition process, FTO glass was cleaned in detergent, isopropanol, ethanol, and deionized water (DI-water) in the ultrasonic cleaning machine for 30 min in sequence. After 3 h of reaction at 25°C, the substrate was taken out and put into a bottle of fresh solution to enable the continual growth of PbS crystal. After another 3 h, the substrate was taken out and washed in deionized water. Then it was blown with an N_2 gas gun until dry. The final film thickness was about 1 μm. Then, the 0.01 mol/L SbF_3/C_2H_5OH solution was dropped on top of the PbS layer and spin-coated at a speed of 3000 r/min for 30 s, followed by thermal annealing at 200°C for 0.5 h. Finally, an aluminum (Al) metal layer with a thickness of 70 nm was evaporated as the top electrode.

RESULTS AND DISCUSSION

Chlorine passivation of PbS film

Photodetectors can be fabricated into three architectures: photoconductors, photodiodes, and phototransistors [26,27]. Photodiodes operate on the built-in electric field formed at the interface of p-type and n-type materials. The built-in electric field suppresses carrier diffusion from both sides and swiftly separates photogenerated carriers once they diffuse into the depletion region. As a result, photodiodes offer low dark current and fast response times, making them ideal for high-speed applications. For p-n junction optoelectronic devices made from the polycrystalline semiconductor film, large grain size, and passivated bulk and surface defects are desirable for improved charge transfer and reduced dark current. Here, we use liquid-phase chemical deposition to fabricate PbS polycrystalline thin films. The chemical solution was prepared with lead nitrate ($Pb(NO_3)_2$), sodium hydroxide (NaOH), and thiourea ($CS(NH_2)_2$). To eliminate the influence of cations, sodium chloride (NaCl) was chosen as an additive to the precursor solution to improve the quality of the PbS film. We added 0.2, 0.5, 5, and 15 mg of NaCl to the precursor solution, respectively. The corresponding molar fraction of chloride ions was 0.96%, 2.4%, 24%, and 72%. To monitor the growth rate, surface morphology, and crystalline properties of the obtained film, six identical FTO substrates were placed in the same deposition bath for each condition. At different times, one substrate was taken out and the film thickness was measured using a step profiler while scanning electron microscope (SEM) and X-ray diffraction (XRD) were used to analyze morphology and crystallinity. The detailed experimental processes are described in the EXPERIMENTAL SECTION. For simplicity, we refer to PbS film without Cl^- as pristine PbS and with Cl^- as Cl-PbS.

The effects of different amounts of NaCl on the growth rate, crystalline orientation, and crystalline size of PbS thin film were summarized in Fig. 1 and Fig. S1. Fig. 1b shows that the crystalline size and the Pb/S atomic ratio of pristine PbS film were approximately 50 nm and 1.31, respectively. As the content of

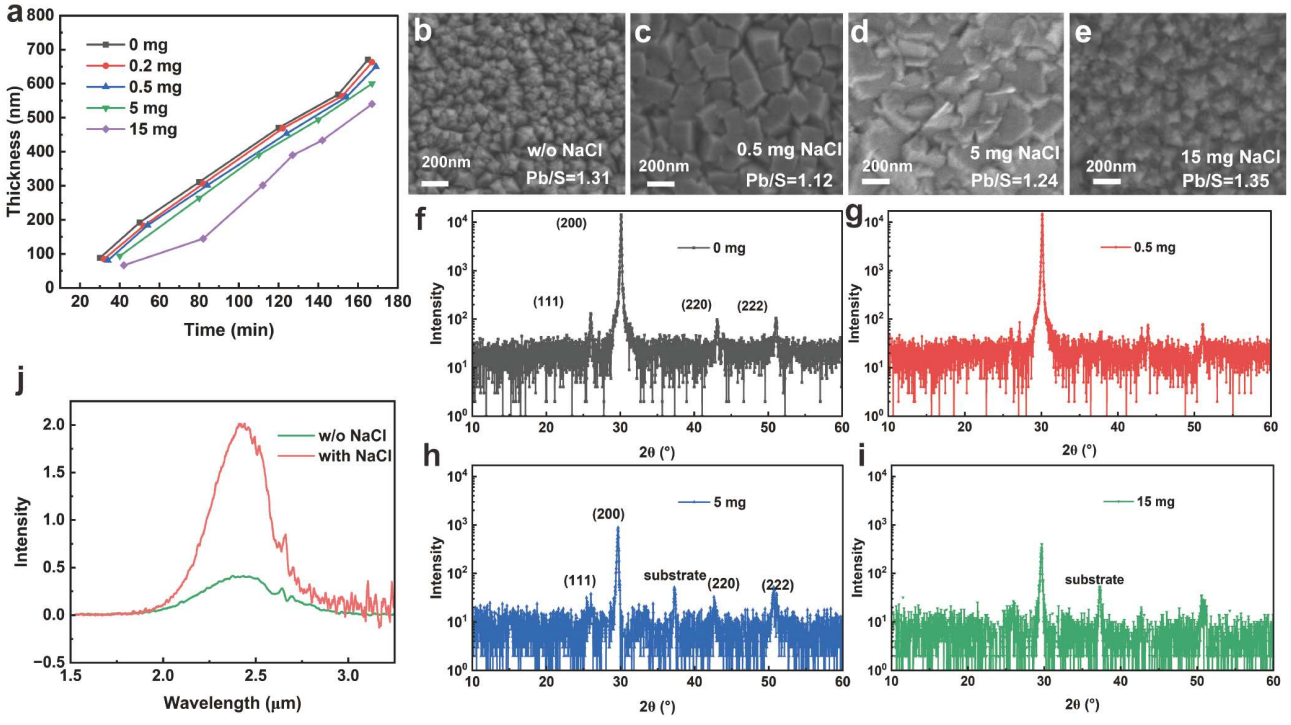

Figure 1 Variation of PbS film thickness with time under different contents of sodium chloride additive (a). SEM image and elements ratio of pristine PbS (b) and Cl-PbS thin film processed under different contents of sodium chloride additive (c–e). XRD at log scale of pristine (f) and Cl-PbS thin film processed under different contents of sodium chloride additive (g–i). PL of pristine and Cl-PbS thin film processed with 0.5 mg sodium chloride additive (j). The PL measurement was conducted at room temperature (298 K) and ambient atmosphere with light excitation under a 980 nm laser.

© Science China Press 2025

NaCl increased from 0.2 to 15 mg, the PbS film growth rate slowed. The slope of the PbS thin film growth rate curve with 0, 0.2, 0.5, 5, and 15 mg additive was 3.97, 3.98, 3.95, 3.92, and 3.87 nm/min, respectively (Fig. 1a). The SEM and XRD measurements indicated that adding 0.2 mg NaCl had little effect on the crystallization of PbS film. The crystallinity and morphology remained comparable to those of the pristine film (Fig. S1). With 0.5 mg NaCl, the crystalline size increased to 200 nm, and the (100) peak intensity became relatively higher than other small peaks. In addition, the Pb/S atomic ratio decreased to 1.12. However, when the content of NaCl increased to 5 mg, the crystallite shape changed significantly and the crystalline size became non-uniform, with smaller crystals embedded between larger ones. At 15 mg NaCl, the crystalline size decreased to less than 30 nm, even smaller than the pristine film. These results suggested that adding 0.5 mg NaCl yielded the best morphology and crystallinity.

We further performed XPS measurements to characterize the Cl-PbS film. As shown in Fig. 2, the existence of Cl^- was confirmed by the local chemical environment of Pb^{2+}. The XPS spectra of Cl-PbS film revealed three fitted peaks at 137.5, 138.6, and 139.4 eV, corresponding to Pb–S, Pb–OH, and Pb–Cl bonds, respectively. The peak at 138.6 eV belongs to the Pb–OH bond rather than the Pb–O bond, as confirmed by the O 1s spectrum, which showed only one peak at 531.4 eV, consistent with Zherebetskyy's report [28]. In comparison, the pristine film exhibited an additional peak at 529.4 eV, which is derived from the Pb–O bond. This result indicated that the chloride additive significantly reduced the oxygen content in the PbS crystal lattice, providing evidence that chloride ions can passivate sulfur vacancy defects (V_s). According to the first-principles calculations by Mishra and Makov [29], the oxygen-in-sulfur (O_s) defect has a negative formation energy (−0.58 eV), creating deep defect states (0.14 eV above the valence band) in the bandgap. However, this process is kinetically limited due to the energetic barrier of oxygen entering PbS. The reduced oxygen substitutional defects suggested that the chloride ions kinetically hindered this process. Additionally, oxygen substitutional defects cause the p-type conductivity behavior of the PbS film. Thus, the reduced Pb–O bond content could be justified by a lower carrier concentration. As shown in Tables S1 and S2, the Hall carrier concentration decreased from 6.41×10^{17} to 2.77×10^{16} cm^{-3}. In addition, larger and purer crystals also indicate higher carrier mobility, as confirmed by the Hall mobility, which improved from 0.7 to 9.1 $cm^2/(V\ s)$.

To verify the passivation of sulfur vacancy defects, the optical and electrical properties of two types of films with the same thickness were measured. First, we conducted the photoluminescence spectrum (PL) measurement. As shown in Fig. 1j, the PL intensity increased from 0.41 to 1.98 with the addition of 0.5 mg NaCl. The full-width at half-maximum (FWHM) decreased from 99 meV in pristine PbS film to 75 meV in Cl-PbS film. Next, we conducted time-resolved microwave conductivity (TRMC) measurements to evaluate the carrier lifetime of PbS film (Fig. S3). The TRMC provides information about both the radiative recombination process and the non-radiative recombination process, which is necessary to evaluate the overall charge carrier lifetime [30]. Fitting the curve with a bi-exponential function (Fig. S3 and Table S3), we found that the overall carrier lifetime increased from 103.3 ns to 2.46 μs with 0.5 mg NaCl, marking a 24-fold improvement. The enhanced PL efficiency and carrier lifetime indicated that the Cl-PbS thin film had a lower defect density. We then measured the temperature-dependent current-voltage characteristics of pristine and Cl-PbS films, by which we could calculate the activation energy of the dark current and deduce the energy depth of related defects. As shown in Fig. 3a, b, the pristine film exhibited an activation energy of 0.14 eV at a high-temperature range, well matching the sulfur vacancy defects, which were absent in the Cl-PbS film. Therefore, we could conclude that the addition of chloride ions improved the crystalline quality of the PbS thin film by reducing the sulfur vacancy defects and increasing the crystal size.

To elucidate the origin of improved crystal quality, from the perspective of the crystal growth mechanism, we proposed that crystal growth is more favorable when chloride ions coordinate with the PbS (100) surface. Sulfur vacancies and oxygen-in-sulfur substitution defects in PbS thin films often arise during chemical solution deposition due to incomplete sulfur incorporation and oxygen contamination from the aqueous environment, especially under high pH conditions. During the deposition process, thin film growth occurred through layer-by-layer ion adsorption. Initially, Pb–OH complexes adsorb onto the substrate, followed by the replacement of OH^- ligands by S^{2-}, which binds to Pb^{2+}. However, in the liquid-phase system, OH^- may remain trapped in the lattice. Besides, OH^- can also coordinate tightly with the PbS crystal surface, halting growth prematurely. This results in smaller grains with a high density of defects, as observed in the pristine film. The introduction of Cl^- induces competition with OH^- ligands. This interaction leads to the rearrangement of surface atom configuration, promoting continued grain growth. This is because OH^- and Cl^- tend to coordinate with the PbS (100) surface with different structures. OH^- is energetically stable with top coordination on one Pb site, while Cl^- tends to coordinate with a bridge configuration between two Pb sites [28]. The diagrams of coordination structures are plotted in Fig. S4. When Cl^- is used as an alternative ligand to coordinate with the PbS (100) surface, the S^{2-} could attack Pb^{2+} much more easily, which is favorable for (100) facet growth, thus leading to a better orientation and larger crystal grain. Therefore, chloride ions compete with oxygen for incorporation, suppressing oxygen-in-sulfur defects. In addition, the ionic radius of Cl^- (176 pm) closely matches that of S^{2-} (179 pm), enabling chloride ions to occupy sulfur vacancy sites without significant lattice distortion. This passivation reduces trap states in the band gap, as confirmed by the decrease in carrier concentration and the increase in carrier lifetime. However, excessive chloride ions in the solution system will consume reactive lead sources and occupy the surface of the PbS crystal. Consequently, the effective concentration of the reactive lead source is reduced and the PbS crystal surface will be capped by chloride ions, thereby impeding the crystal growth.

Performance of PbS homojunction photodiode

We measured the absorption spectra of PbS thin film by Fourier transform infrared absorption spectroscopy. The absorption coefficient (α), calculated from the absorption spectrum, is shown in Fig. S5. The optical bandgap was calculated as 0.46 eV via the Tauc plot method, close to the reported range of 0.42–0.45 eV. At 2.3 μm, α was found to be 1.00×10^4 cm^{-1}, indicating that photons with energy of 0.54 eV can be fully absorbed in a 1 μm thickness PbS film. We determined energy band levels using ultraviolet photoelectron spectroscopy (UPS) measure-

 © Science China Press 2025

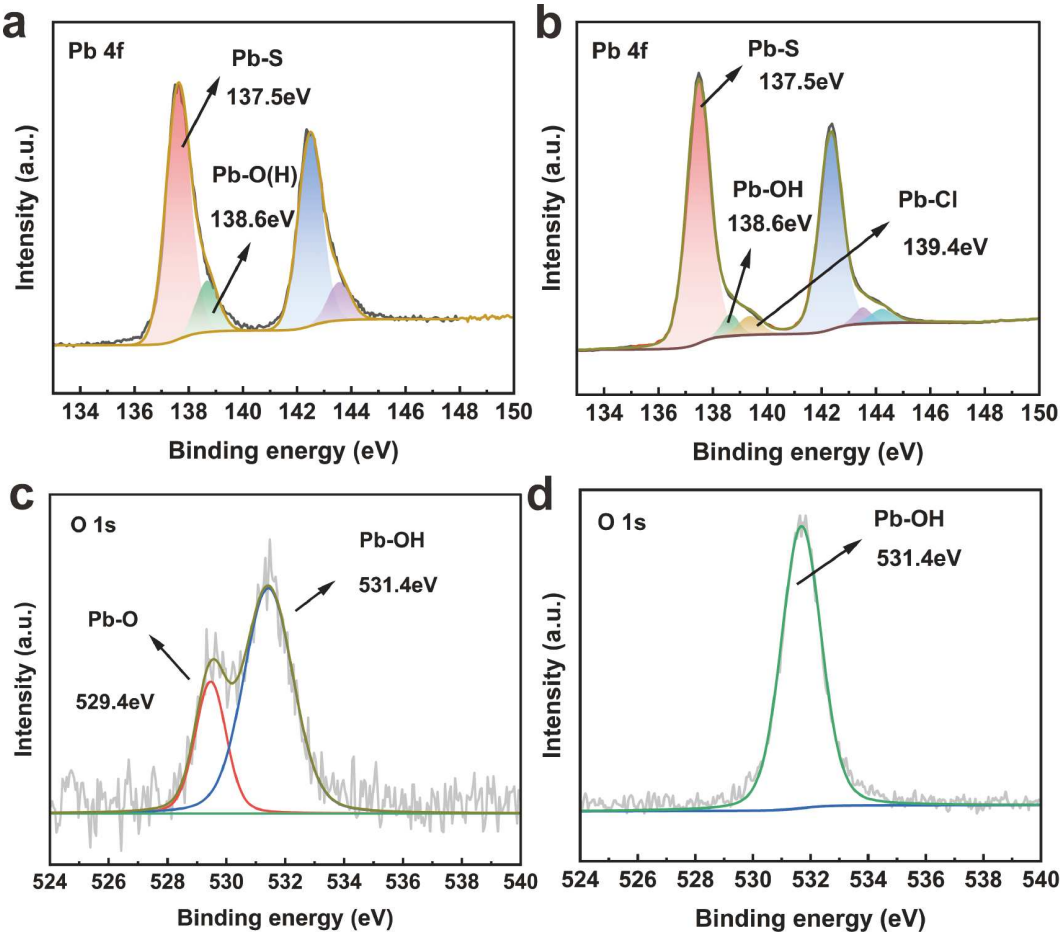

Figure 2 XPS measurements of the PbS thin film. The fitted Pb 4f (a) and O 1s (c) spectra of the pristine PbS thin film. The fitted Pb 4f (b) and O 1s (d) spectra of Cl-PbS thin film with 0.5 mg sodium chloride additive.

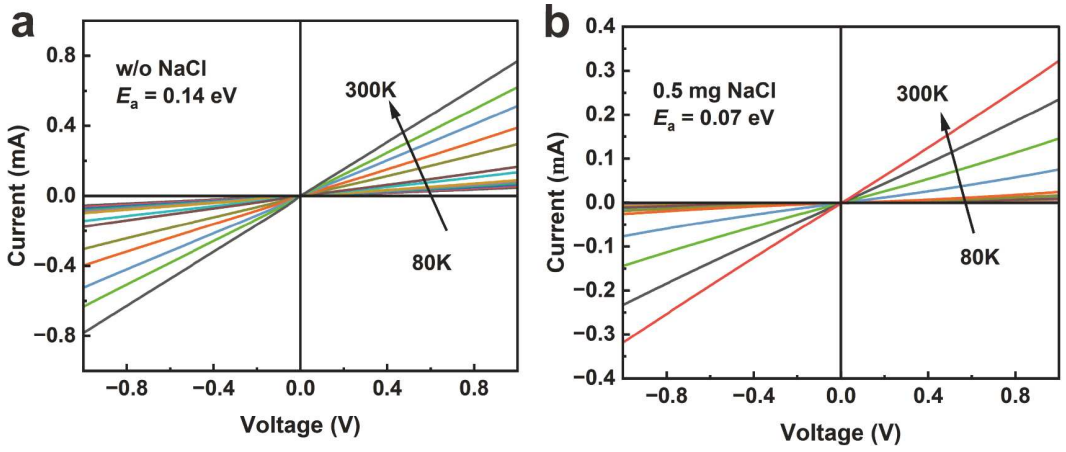

Figure 3 Temperature-dependent current-voltage characteristics of pristine PbS (a) and Cl-PbS (b) thin films. The measurements were conducted under dark conditions.

ment. The Fermi level was −4.55 eV, calculated from a cut-off energy of 16.67 eV. The valence band maximum (VBM) was −4.75 eV, derived from a cut-off energy of 0.20 eV. Combined with the optical bandgap, the conduction band minimum (CBM) of −4.29 eV was obtained.

The homojunction photodetector was fabricated as an n-on-p device structure. Two layers of PbS thin film, with a total thickness of about 1 μm, were first deposited on FTO glass (Fig. S5). Subsequently, the SbF_3/C_2H_5OH solution was spin-coated on the PbS thin film, followed by thermal annealing at 200°C. This process allows Sb^{3+} to diffuse into the PbS film and form a gradient n-type doping. Finally, a shallow work-function aluminum (Al) metal was evaporated as a top electrode to form an ohmic contact with n-type PbS.

We conducted Hall measurements to verify the n-type nature of SbF_3-doped PbS. The carrier concentration was approximately

 © Science China Press 2025

-1.04×10^{18} cm^{-3}, compared to 2.77×10^{16} cm^{-3} for the undoped film. Fig. 4a, b show the diagram of the homojunction photodiode structure, and element distribution of this device, determined by secondary ion mass spectrometry (SIMS) analysis. The Pb^{2+} and S^{2-} were uniformly distributed in the film. The distribution of Sb^{3+} complied well with the typical Gaussian distribution model resulting from the thermal diffusion process, indicating a gradient junction.

Dark current density is a key parameter for photodetectors, which determines the shot noise of the photodiode and thus detectivity. Fig. 4c presents the current density-voltage (*J*-*V*) characteristics measured at 300 K in the dark and under 1.3 μm illumination with an intensity of 340 μW/cm^2. The homojunction photodiode exhibited a rectification ratio of over 100 at ±1 V. The dark current density of the Cl-PbS photodiode at 0 V was 3.1 μA/cm^2, which was slightly higher than that of the pristine PbS photodiode but three times lower under higher bias voltage. At −0.01 V, the dark current density of the Cl-PbS photodiode was 0.00105 A/cm^2, compared to 0.0045 A/cm^2 for the pristine PbS photodiode.

The external quantum efficiency (EQE) and spectral responsivity of the Cl-PbS photodiode at different wavelengths are shown in Fig. 4d. The EQE and responsivity at 2.5 μm were 39.3% and 0.79 A/W, respectively. With the increase of incident light wavelength, the light intensity penetrated deeper into the active layer and the photoexcited carriers were produced near the depleted region. Therefore, the photoexcited carriers were collected more efficiently, resulting in higher responsivity at 2.5 μm compared to shorter wavelengths. Fig. 4e shows the measured noise characteristics of the Cl-PbS photodiode. Among the three types of noise affecting the specific detectivity *D**, the Johnson noise dominated the shot noise and *1/f* noise at high frequency. At 1 kHz, the *D** at 2.5 μm could be calculated as 8.79×10^9 cm Hz$^{1/2}$/W at 0 V, according to Equation (1), where *R*, Δ*f*, *A* and i_n are the responsivity, bandwidth, device area, and noise current [30]. In Table 1, we summarize the performance of reported PbS photodiodes. The Cl-PbS homojunction photodiode exhibited the best specific detectivity among these photodiodes.

$$D^* = \frac{R\sqrt{\Delta f\, A}}{i_n}, \tag{1}$$

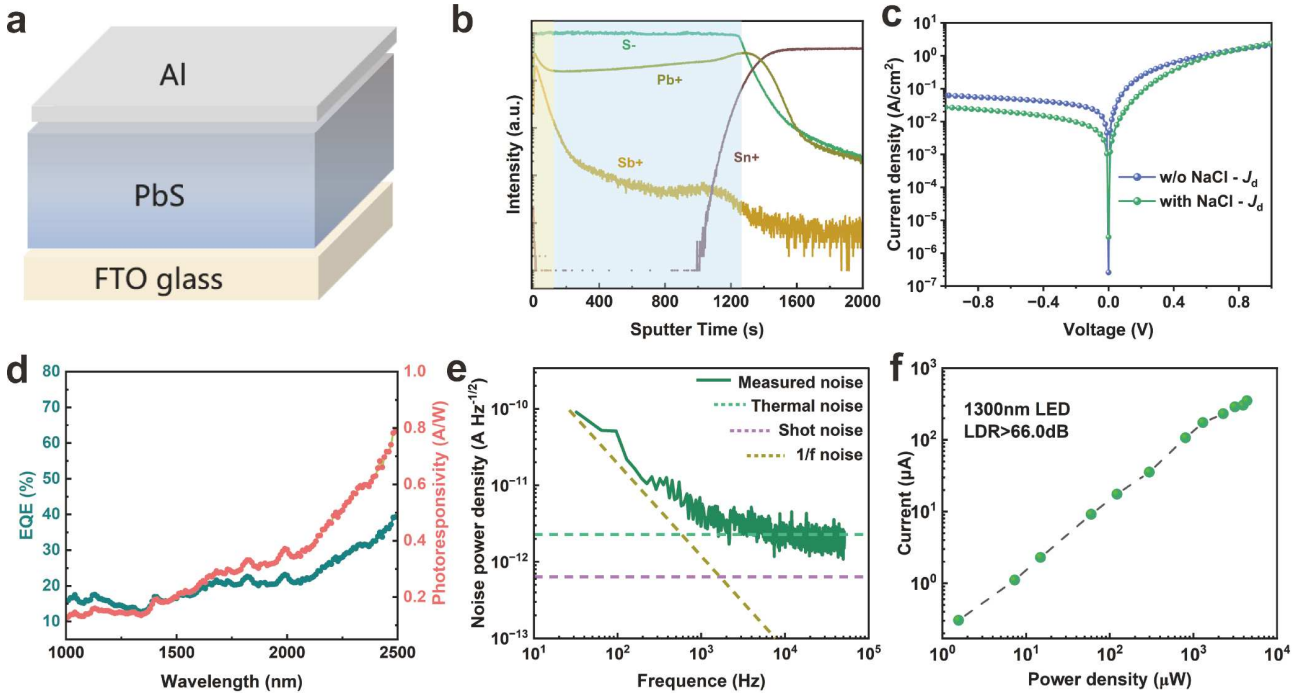

Figure 4 (a) Homojunction device structure diagram; (b) SIMS analysis of Cl-PbS homojunction photodiode; (c) dark current density-voltage (J_d-*V*) of two different devices fabricated by PbS film with or without Cl^- passivation (d-dark); (d) room temperature response spectrum and EQE at 0 V of PbS photodiode made by Cl-PbS film; (e) measured noise current at different frequencies at 0 V bias of PbS photodiode made by the Cl-PbS film. The calculated shot noise, 1/*f* noise, and generation-recombination (G-R) noise limit are also included for reference; (f) linear dynamic range of Cl-PbS photodiode.

Table 1 Performance of several classical PbS bulk thin film photodiodes

Photodiodes	Wavelength (nm)	Temperature (K)	*D** (Jones)	Ref.
PbS/Si	1300	300	4.4×10^9	[31]
PbS/Si	1550	300	1.3×10^9	[32]
PbS/Si	3000	200	10^{10}	[18]
PbS/GaAs	3200	77	2.0×10^9	[22]
PbS/PbS(Sb)	2550	300	4.8×10^9	[24]
Cl-PbS/PbS(Sb)	2500	300	8.79×10^9	This work

© Science China Press 2025

$$\mathrm{LDR} = 20\log\left(\frac{P_{\max}}{P_{\min}}\right). \quad (2)$$

Using a 1.3 μm LED as a light source, the linear dynamic range (LDR) of the Cl-PbS photodiode was investigated. The LDR was over 66 dB (Fig. 4f), calculated according to Equation (2), where P_{max} and P_{min} are the maximum and minimum power density in the linear region of photocurrent versus power density (I_p-P_{light}) log curve. The transient response was measured by a high-speed oscilloscope, finding rising and falling times of 19.6 and 23.7 μs, respectively (Fig. S6).

Dark current analysis of PbS homojunction photodiode

To further evaluate the quality of PbS homojunction, we have conducted electrical measurements to investigate the defect physics and identify the components of dark current. From the temperature-dependent *J*-*V* measurements, the defect activation energy at different reverse biases could be estimated. According to how different dark current components relate to E_g and bias voltage (Equations (3)–(5)), we can identify the main contributions of total dark current. If $E_a = E_g$ ($n = 1$), the dominant dark current is diffusion current (J_{diff}) arising from thermally activated carriers in the neutral region. The diffusion current varies with temperature and is almost independent of bias voltage; if $E_a = E_g/2$ ($n = 2$), the dominant dark current is generation current ($J_{G\text{-}R}$) arising from recombination center in junction region or ohmic current from shunt resistance. The generation current increases exponentially with the increase of bias voltage, but ohmic current increases linearly with voltage [33]. The temperature-dependent *J*-*V* characteristics, voltage-dependent E_a, fitted dark current, and quality factors are shown in Fig. 5. The activation energy E_a at different reverse biases was calculated according to the Arrhenius equation. The results are summarized in Table S4.

$$J_{\mathrm{diff}} = J_{\mathrm{diff,sat}}(\mathrm{e}^{-eV/k_{\mathrm{B}}T} - 1), \quad (3)$$

$$J_{\mathrm{G\text{-}R}} = \frac{qn_{\mathrm{i}}W_{\mathrm{d}}}{2\tau_{\mathrm{eff}}}(\mathrm{e}^{-eV/2k_{\mathrm{B}}T} - 1), \quad (4)$$

$$J \propto A\mathrm{e}^{-qV/nk_{\mathrm{B}}T}, \quad (5)$$

$$J_{\mathrm{d}} = J_0\left(\mathrm{e}^{\frac{e}{k_{\mathrm{B}}T}(V-J_{\mathrm{d}}R_{\mathrm{s}})} - 1\right) + \frac{V-J_{\mathrm{d}}R_{\mathrm{s}}}{R_{\mathrm{sh}}} + k(V-J_{\mathrm{d}}R_{\mathrm{s}})^m, \quad (6)$$

where J_{diff} and $J_{G\text{-}R}$ represent diffusion current and generation-recombination current, respectively. J_d is the dark current density; V is the applied voltage bias; J_0 is the reverse saturation current density of the diode; n is the ideality factor; e is the elementary charge; k_B is the Boltzmann constant; T is the temperature; R_s is the series resistance; R_{sh} is the shunt resistance; k and m are constants related to non-Ohmic leakage current.

Based on the fitted J_d-V characteristics of the Cl-PbS photodiode (Fig. 5c) and pristine PbS photodiode (Fig. S7), the reverse saturation current and non-ohmic leakage current of the Cl-PbS photodiode were significantly reduced. This can be ascribed to the reduced oxygen defect densities in the Cl-PbS thin film. The O_s defect is shallow and can cause large trap-assisted tunneling

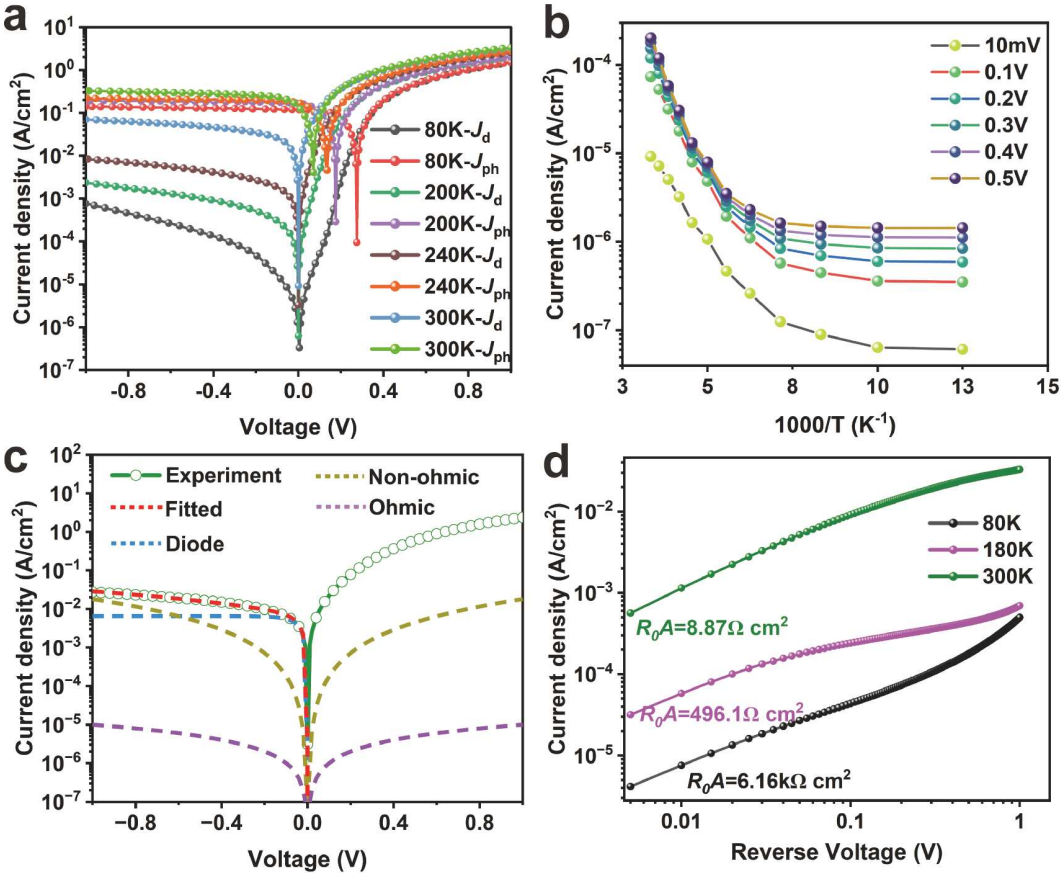

Figure 5 Temperature-dependent current density-voltage measurement (d-dark, ph-light) (a); activation energy under different reverse bias (b); reverse current density-voltage characteristic and fitted dark current components at different reverse voltages under room temperature (c); calculated quality factor R_0A at different temperatures of Cl-PbS homojunction photodiode (d).

© Science China Press 2025

current even at low bias. Non-Ohmic leakage can be attributed to trap-assisted tunneling current and interface defects [34]. From reverse bias characteristics, we could determine the dependence of activation energy E_a on voltage. In the high-temperature range (200–300 K), E_a increased gradually from 0.109 eV at −10 mV to 0.172 eV at −0.5 V. The E_a showed a positive dependence on voltage, and was lower than $E_g/2$ of PbS (0.23 eV), suggesting that trap-assisted tunneling current contributed significantly to a large dark current at higher voltages [35,36]. This may arise from the grain boundaries in the PbS polycrystalline thin film. From the J_d-V characteristics, the quality factors R_0A of the PbS photodiode at different temperatures can be calculated. At 80 and 300 K, R_0A values were 6.16 kΩ cm^2 and 8.78 Ω cm^2, respectively.

CONCLUSIONS

In summary, we demonstrated the first use of chloride ions to passivate *in situ* the sulfur-related defects of liquid-phase chemical-deposited PbS polycrystalline film. The oxygen-in-sulfur defects were almost eliminated and the Pb/S atomic ratio was greatly reduced to near-unity. Consequently, the overall carrier lifetime increased over 20-fold, and photoluminescence full-width at half-maximum decreased to 75 meV. Owing to the reduced bulk defect densities, the p-n homojunction photodiode exhibited a responsivity of 0.79 A/W at 2.5 μm and a linear dynamic range of over 66 dB. The dark current density was 3.1 μA/cm^2 at 0 V, corresponding to a specific detectivity of 8.79 × 10^9 cm Hz$^{1/2}$/W at 2.5 μm, which was among the best reported lead sulfide bulk thin film photodiodes. We also identified trap-assisted tunneling current as the primary dark current component, likely due to grain boundaries in the PbS thin film.

Received 14 May 2025; accepted 21 June 2025; published online 8 September 2025

1 Herschel W. II. Experiments on the refrangibility of the invisible rays of the Sun. Philo Mag, 1800, 8: 9–15
2 Arnquist WN. Survey of early infrared developments. Proc IRE, 1959, 47: 1420–1430
3 Rogalski A. History of infrared detectors. Opto-Electron Rev, 2012, 20:
4 Case TW. Notes on the change of resistance of certain substances in light. Phys Rev, 1917, 9: 305–310
5 Kutzscher EW. Review on detectors of infrared radiation. Electro-Opt Syst Design, 1974, 6: 30–34
6 Tidhar GA, Segal R. New applications with a SWIR imager employing extended wavelengths. In: SPIE 8012, Infrared Technology and Applications XXXVII. Orlando: SPIE, 2011. 801207
7 Elabd H, Steckl AJ. Abstract: growth of polycrystalline PbS films. J Vacuum Sci Tech, 1978, 15: 264
8 Nykänen E, Laine-Ylijoki J, Soininen P, *et al.* Growth of PbS thin films from novel precursors by atomic layer epitaxy. J Mater Chem, 1994, 4: 1409–1412
9 Atwa DMM, Azzouz IM, Badr Y. Optical, structural and optoelectronic properties of pulsed laser deposition PbS thin film. Appl Phys B, 2011, 103: 161–164
10 Wang Y, Xia J, Li X, *et al.* Vapor phase epitaxy of PbS single-crystal films on water-soluble substrates and application to photodetectors. Nano Res, 2022, 15: 5402–5409
11 Isshiki M, Endo T, Masumoto K, *et al.* Epitaxial growth of PbS thin films from aqueous solution. J Electrochem Soc, 1990, 137: 2697–2700
12 Qiu J, Liu Y, Zhang G, *et al.* Modified vapor phase deposition technology for high-performance uncooled MIR PbSe detectors. RSC Adv, 2021, 11: 34908–34914
13 García de Arquer FP, Armin A, Meredith P, *et al.* Solution-processed semiconductors for next-generation photodetectors. Nat Rev Mater, 2017, 2: 16100
14 Feng X, Li C, Song J, *et al.* Differential perovskite hemispherical photodetector for intelligent imaging and location tracking. Nat Commun, 2024, 15: 577
15 Zhou Y, Sun Z, Ding Y, *et al.* An ultrawide field-of-view pinhole compound eye using hemispherical nanowire array for robot vision. Sci Robot, 2024, 9: eadi8666
16 Gu L, Poddar S, Lin Y, *et al.* A biomimetic eye with a hemispherical perovskite nanowire array retina. Nature, 2020, 581: 278–282
17 Phan H, Yi J, Bae J, *et al.* Artificial compound eye systems and their application: a review. Micromachines, 2021, 12: 847–875
18 Davis JL, Norr MK. Ge-epitaxial-PbS heterojunctions. J Appl Phys, 1966, 37: 1670–1674
19 Rahnamai H, Gray HJ, Zemel JN. The PbS–Si heterojunction I: growth and structure of PbS films on silicon. Thin Solid Films, 1980, 69: 347–350
20 Rahnamai H, Zemel JN. The PbS–Si heterojunction II: electrical properties. Thin Solid Films, 1980, 74: 17–22
21 Rahnamai H, Zemel JN. The PbS–Si heterojunction III: optical properties. Thin Solid Films, 1980, 74: 23–27
22 Steckl AJ, Elabd H, Ka-Yee Tam H, *et al.* The optical and detector properties of the PbS-Si heterojunction. IEEE Trans Electron Devices, 1980, 27: 126–133
23 Bernabucci F, Margaritondo G, Migliorato P, *et al.* Near-IR detection by PbS-GaAs heterojunctions. Phys Stat Sol (a), 1973, 15: 621–627
24 Liu Z, Kim JH, Fernandes GE, *et al.* Room temperature photocurrent response of PbS/InP heterojunction. Appl Phys Lett, 2009, 95: 231113
25 Donnelly JP, Harman TC, Foyt AG, *et al.* PbS photodiodes fabricated by Sb^+ ion implantation. Solid-State Electron, 1973, 16: 529–534
26 Yan T, Yang W, Wu L, *et al.* High-work-function transparent electrode with an enhanced air-stable conductivity based on AgNiCu core-shell nanowires for Schottky photodiode. J Mater Sci Tech, 2025, 209: 95–102
27 Deng M, Fang X. 2D perovskite oxides toward high-performance ultraviolet photodetection. Acc Mater Res, 2025, 6: 615–626
28 Zherebetskyy D, Scheele M, Zhang Y, *et al.* Hydroxylation of the surface of PbS nanocrystals passivated with oleic acid. Science, 2014, 344: 1380–1384
29 Mishra N, Makov G. Point defects in lead sulfide: a first-principles study. Comput Mater Sci, 2021, 190: 110285
30 Li Y, Jia Z, Yang Y, *et al.* Shallow traps-induced ultra-long lifetime of metal halide perovskites probed with light-biased time-resolved microwave conductivity. Appl Phys Rev, 2023, 10: 011406
31 Xiao Y, Xu T, Zhang M, *et al.* Study of the quasi-single crystalline lead sulfide film deposited by magnetron sputtering and its infrared detecting characteristics. J Mater Sci-Mater Electron, 2022, 33: 16029–16044
32 Zhang X, Yang C, Li P, *et al.* Growth of Si/PbS heterostructure infrared photodetectors for NIR detection. ACS Photonics, 2024, 11: 1197–1204
33 Gong X, Tong M, Xia Y, *et al.* High-detectivity polymer photodetectors with spectral response from 300 nm to 1450 nm. Science, 2009, 325: 1665–1667
34 Kirchartz T, Deledalle F, Tuladhar PS, *et al.* On the differences between dark and light ideality factor in polymer: fullerene solar cells. J Phys Chem Lett, 2013, 4: 2371–2376
35 Wang Y, Peng L, Schreier J, *et al.* Silver telluride colloidal quantum dot infrared photodetectors and image sensors. Nat Photon, 2024, 18: 236–242
36 Breitenstein O, Altermatt P, Ramspeck K, *et al.* The origin of ideality factors $n > 2$ of shunts and surfaces in the dark I-V curves of Si solar cells. In: the 21st European Photovoltaic Solar Energy Conference. Dresden: European Photovoltaic Solar Energy Society, 2006

Acknowledgement This work was supported by the National Key Research and Development Program of China (2024YFA1209503, 2021YFB3501800), the National Natural Science Foundation of China (62322505, 62374069), and the Innovation Project of Optics Valley Laboratory (OVL2023ZD002). We thank Wenyu Zhang and Ruiming Li for their help in acquiring the TRMC and for helpful discussions regarding TRMC analysis.

 © Science China Press 2025

Author contributions Xu S designed the idea and conducted the synthesis, characterization, and analysis of samples as well as the writing of the original draft. Li S provided the synthesis methods and data analysis of pristine samples. Zhang W and Li R provided the acquisition of TRMC data and analysis. Luo H participated in the discussion of the data analysis; Song H supervised the project; Luo J supervised the project and edited the original draft; Tang J supervised the project and provided the experiment and characterization resources.

Conflict of interest The authors declare that they have no conflict of interest.

Supplementary information Supplementary materials are available in the online version of the paper.

Shaoheng Xu is currently a PhD student at the Wuhan National Laboratory for Optoelectronics, Huazhong University of Science and Technology. He received his Bachelor's degree from Zhengzhou University. His research focuses on the application of lead-based semiconductors in infrared sensors and advanced displays.

Jiajun Luo is a professor at the Wuhan National Laboratory for Optoelectronics, Huazhong University of Science and Technology. Prof. Luo received his PhD degree from Huazhong University of Science and Technology. His research covers a wide range of topics related to optoelectronic displays and sensors from materials to applications.

Jiang Tang is the professor and dean of the School of Optics and Electronic Information, Huazhong University of Science and Technology, and the deputy director of Wuhan National Laboratory for Optoelectronics. He received his doctoral degree from the University of Toronto in Canada. His main research areas include quantum dot infrared image sensors, halide perovskite X-ray detectors, halide perovskite luminescent materials and devices, and thin film solar cells.

氯离子钝化硫化铅薄膜用于高性能拓展波长短波红外探测器

许少恒[1†], 李森[1,2†], 张闻宇[3], 罗浩[4], 李睿明[5], 林乾乾[5], 宋海胜[1], 罗家俊[1*], 唐江[1,2,3,6*]

摘要 化学液相沉积的硫化铅作为一种典型的窄带隙半导体, 在扩展短波红外(2–3 μm)传感领域具有巨大潜力. 然而, 硫化铅薄膜在化学液相沉积过程中通常会产生大量的硫空位和氧杂质, 导致器件性能较差. 本文报道了在液相化学沉积过程中通过添加氯化物实现硫化铅晶粒的原位钝化. 氯离子作为与氢氧根离子竞争的配体, 可以调节硫化铅晶粒的生长, 能够有效降低硫化铅中的硫空位缺陷和氧杂质含量. 此外, 氯离子由于与硫离子的离子半径相近, 占据硫空位不会引起显著的晶格畸变. 因此, 添加氯化物的溶液中得到的硫化铅薄膜具有较低的缺陷密度. 由于体缺陷的减少, 由硫化铅薄膜制备的同质结光电二极管在2.5 μm处表现出0.79 A/W的高响应度以及19.6 μs的快速响应. 在室温下, 1 mm^2的光电二极管的零偏电阻-面积积(R_0A)为8.78 Ω cm^2, 其在2.5 μm处的比探测率为8.79 × 10^9 Jones, 这一性能属于硫化铅薄膜光电二极管中报道的最佳水平之一. 在80 K下, 零偏电阻-面积积达到6.16 kΩ cm^2. 本研究为低成本、高性能扩展短波红外光电探测器的开发提供了一种新思路.

 © Science China Press 2025